Simulation of an Autonomous Surface Vehicle With Colocated Tidal Turbine

Linnea Weicht, Sarmad Hanif, *Senior Member, IEEE*, Craig Bakker, *Member, IEEE*, Taiping Wang, Nolann Williams, and Robert J. Cavagnaro, *Member, IEEE*

***Abstract*—Utility-class autonomous surface vehicles (ASVs) are small watercraft that can be equipped with environmental sensors used to collect data in coastal and marine locations. Their operation is constrained by energy storage limits, but with adequate resources, marine energy presents an opportunity to provide power in remote locations. To demonstrate the feasibility of using tidal energy to support ASV operations, we created a MATLAB-Simulink modeling tool. The model simulates an ASV performing surveys and charging at a nearby tidal turbine. Model components include the tidal turbine, generator, battery storage dynamics, ASV kinetics, and ASV control schemes. We refined the tool using experimentally collected data in the tidal-resource-rich Sequim Bay, which has been proposed for tidal energy testing, to empirically identify vehicle hydrodynamic drag and inertial coefficients. We then used the model to simulate a resource characterization survey in Sequim Bay under varying environmental conditions and survey parameters. Results indicated that a tidal turbine can support continuous ASV operation in low tidal or low target survey speed scenarios, and we suggest improvements to the model.**

***Index Terms*—Autonomous surface vehicle (ASV), MATLAB-Simulink, marine energy, tidal power.**

ASV Model Nomenclature

Variable	*Meaning*
x_{asv}	ASV position vector
v_{asv}	ASV velocity vector in global coordinates.
v_x	ASV surge component velocity.
v_y	ASV sway component velocity.
$\tilde{v}_{\text{asv}}$	ASV velocity vector in local coordinates.
m	ASV mass, including added mass.
M	Additional weight due to accelerating water around the ASV.
θ_{asv}	ASV orientation angle.
ω_{asv}	ASV angular velocity.
T	Thrust in the ASV surge direction.
v_{curr}	Surface current velocity vector
C_D	Experimentally determined ASV surge drag coefficient.
$C_{D,x}$	Drag force coefficient in ASV surge direction (including area and fluid density)
$C_{D,y}$	Drag force coefficient in ASV sway direction (including area and fluid density)
C_m	Added mass coefficient.
I_z	ASV moment of inertia about the z-axis.
τ	Torque.
$C_{D,\tau}$	Rotational drag coefficient (kg/m^2)
F_D	Drag force in global coordinates.
$\tilde{F}_D$	Drag force in ASV local coordinates.
$F_{D,\tau}$	Drag force, rotational.
I_{bat}	Current draw from ASV battery.
V_{bat}	ASV battery voltage.
$\theta_{\text{target}-\text{asv}}$	ASV target heading.
η	Combined battery, motor, and thruster/propeller efficiency.
s_{asv}	ASV relative speed.
$v_{\text{target}-\text{global}}$	ASV target velocity over ground.
$v_{\text{target}-\text{asv}}$	ASV target velocity.
P	Mechanical power of ASV moving through water.
P_{bat}	Power recorded leaving ASV battery.
F_{hyd}	Hydrodynamic force on ASV due to added mass and drag.
F_{Cm}	Force on ASV due to to added mass.
ρ	Fluid density.
V_{asv}	Volume of the ASV underwater.

Received 26 September 2023; revised 2 May 2024; accepted 3 July 2024. This work was supported in part by the Pacific Northwest National Laboratory, operated by Battelle Memorial Institute for the U.S. Department of Energy (DOE), under Grant DE-AC05-76RL01830, in part by the U.S. Department of Energy Office of Energy Efficiency, and in part by the Renewable Energy Water Power Technologies Office. *(Corresponding author: Linnea Weicht.)*

Associate Editor: K. Takagi.

Linnea Weicht, Craig Bakker, Taiping Wang, and Robert J. Cavagnaro are with the Pacific Northwest National Laboratory, Richland, WA 99354 USA (e-mail: linnea.weicht@pnnl.gov; craig.bakker@pnnl.gov; Taiping.Wang@pnnl.gov; robert.cavagnaro@pnnl.gov).

Sarmad Hanif was with the Pacific Northwest National Laboratory, Richland, WA 99354 USA. He is now with Electric Power Research Institute, Palo Alto, CA 94304 USA (e-mail: SHanif@epri.com).

Nolann Williams was with the Pacific Northwest National Laboratory, Richland, WA 99354 USA. He is now with A-M Systems, Sequim, WA 98382 USA (e-mail: nwilliams@borealisblue.com).

Digital Object Identifier 10.1109/JOE.2024.3428605

I. Introduction

AUTONOMOUS and uncrewed vehicles are an important tool for coastal ocean monitoring, both under water and on the surface, and they have revolutionized the way in which we study critical ocean variables. Adoption of robotic platforms, such as autonomous underwater vehicles (AUVs), drifting profiling floats, and buoyancy gliders, has been rapid and continues to expand. Automated ocean-observing technology, primarily in the form of AUVs, transitioned from research to broad coastal ocean science use in the early 2000s, when commercially available vehicles that can be integrated with a diverse array of sensors were demonstrated to perform with accuracy and consistency [1]. Such platforms offer the ability to survey in

places and ways that a crewed research vessel could not and with potential cost savings, higher precision, and lower risk to human health.

Autonomous surface vehicles (ASVs) used for ocean observing are similar to traditional crewed research vessels in that they have similar capabilities, but they come in a much smaller package. They benefit from having properties similar to AUVs for coastal surveys, including access to shallower areas, precision positioning, and the ability to integrate sensing and control elements. They also enable access to challenging environments where risk of loss is high, may be deployed in groups or swarms for coordinated operation, and allow observations closer to the sea surface without the impacts of the motion of a larger platform [2]. ASVs may have endurance on the order of hours [3] to months [4] depending on vehicle size, energy source, speed of operation, and sensor payload; the range of technology in use is diverse. Additional dual-modal unmanned vehicles have been proposed that allow for movement at the ocean surface and at depth, which face similarly challenging deployment duration constraints [5], [6].

Uncrewed marine vessels have advanced in the last decades as their use has become more widespread. Recent technology development has focused on overcoming limitations imposed on the platforms by energy constraints that restrict mission duration and available power for sensors and communications. Integrating energy-harvesting elements can provide additional electrical or mechanical power for propulsion or storage. The feasibility of wave power for recharging has been investigated for AUVs with results that indicate potential for increased mission duration [7], [8]. The WaveGlider and Saildrone use power from waves and wind, respectively, to extend duration, often by months, by directly powering propulsion. They also feature solar photovoltaic units at the surface to support control and sensing loads [9], [10]. While these technologies use marine energy, they are not well-suited for coastal operations, where environmental monitoring may be desired. More traditionally propelled ASVs (e.g., using thrusters or propellers) better suited for nearshore coastal environments featuring solar panels and wind turbines have been developed to increase mission duration and capability [11], [12].

With these recent advances in autonomous vehicle technology and improvements in oceanographic sensors, satellite communications, and platform coordination, a concept of continuous and widespread in situ operation of ocean-observing systems is becoming realistic [13]. Each of these advances will require more access to energy that will need to come from onboard storage, a cabled connection to the power grid or a standalone generating system, or the surrounding environment. Solar photovoltaic, offshore wind, wave, current, and thermal gradient energy resources and associated technologies are candidates for enabling continuous autonomous vehicle operation, and waves and currents potentially offer the highest energy density [13]. Marine energy technologies, particularly wave and tidal energy converters, have the potential to deliver significant power for a variety of ocean observing use cases in locations where strong resources exist [14].

In this work, we present a concept and analysis of a use case for resident or continuous operation of an ASV powered by tidal energy in a dynamic coastal environment. Sequim Bay, WA, USA, features a swift tidal channel at its inlet and the Pacific Northwest National Laboratory's (PNNL's) Marine and Coastal Research Laboratory (MCRL) adjacent to it. The bay contains many natural features, and their continuous monitoring would enhance understanding of nearshore oceanographic processes. For example, continuously monitoring eelgrass beds, which are critical habitat for many fish and invertebrates as well as being key constituents of the blue carbon cycle [15], enables tracking of the impacts of changing climate properties on their growth and ability to sequester carbon. Such a monitoring campaign is well-suited for automation using a small ASV because it requires repeated and precise multiparameter measurement, is in a shallow water zone unsuitable for a crewed research vessel or AUV, and extends over a large area unsuitable for fixed monitoring assets. A state-of-the-art approach to conducting this measurement campaign with an ASV would require a dedicated crew to repeatedly deploy, recover, and recharge the ASV. We propose augmenting an ASV's capabilities with the ability to recharge from a docking platform that harvests tidal energy with a hydrokinetic turbine at the site. Such a setup would further automate this type of measurement campaign, use an energy resource that does not emit carbon dioxide, and allow for operation in areas that may be far from a grid connection for charging.

Here, we demonstrate the feasibility of powering ASV operations with tidal energy by simulating a use case, including energy harvesting, ASV path planning, motion through dynamic tidal current, and accounting for energy utilization. Our approach endeavors to model the dynamics of each critical subsystem (turbine, generator, energy storage, ASV motion, etc.) in a single simulation environment. Numerical simulation of autonomous vehicles has been accomplished in a wide variety of ways for different objectives [16]. Many approaches create highly accurate models (e.g., as in [17]) for testing aspects like the efficacy of a control strategy. Others use simulation environments built to run in the same operating system common to robot control (i.e., Gazebo/Robot Operating System) [18]. In comparison with these methods, the simulation we describe is purpose-built for coupling energy harvesting with vehicle operations.

II. Methods

A. Modeling Framework

Simulation of an ASV with a colocated energy-harvesting use case is complex and requires the coupling of spatiotemporally varying environmental fluid flow, ASV motion and energy consumption, turbine operation, and energy harvesting and storage. To accommodate the variety of distinct physical processes involved, we developed models of a tidal turbine, generator, and battery storage, and vehicle in the Mathworks MATLAB-Simulink environment. MATLAB and Simulink 2020b were used to run the model on a PC with 16 GB installed physical memory (RAM) and an Intel Core i7-8665U processor. An overview of the system is depicted in Fig. 1. Each subsystem model was built as an individual code block and then combined into a single Simulink model to allow for swift reconfiguration. We designed an additional path planning module as a MATLAB

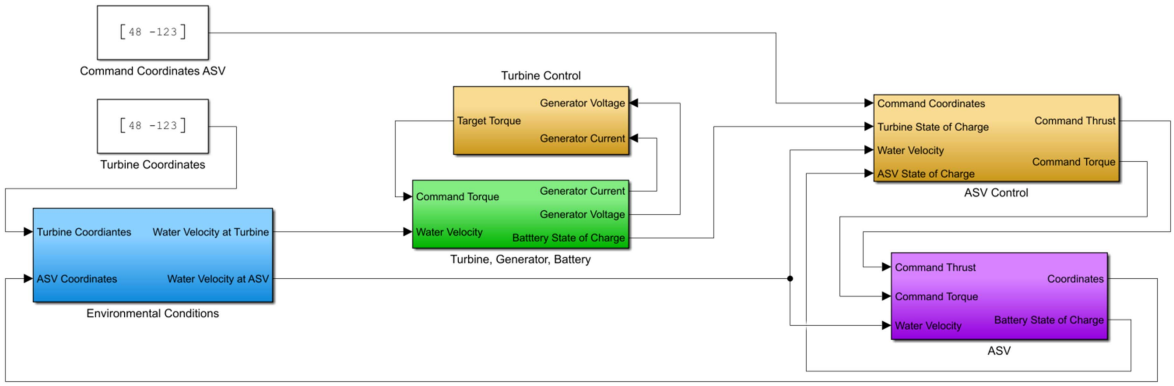

Fig. 1. Block diagram of MATLAB-Simulink model.

script; this script represents the pre-mission planning commonly performed during ASV operations. Environmental data used to bound and force the simulation (i.e., geography, bathymetry, and precompiled water surface velocity throughout the simulation domain) for our use case location in Sequim Bay, WA, were stored in a MATLAB scattered interpolant object queried at each time step. The objective driving the modeling approach is accurate simulation of the use case systems to determine the feasibility of the concept of operation and to serve as a design tool for these systems. The following sections describe the construction of each simulation module.

1) Hydrodynamic Flow Model: The turbine and ASV motion blocks within the Simulink model rely on input current velocities driven by tidal forcing, which are output using PNNL's hydrodynamic model of Sequim Bay. The hydrodynamic model is a standalone model developed from PNNL's Finite Volume Coastal Ocean Model-based (FVCOM-based) Salish Sea Model by significantly refining grid resolutions in the Sequim Bay area [19], [20]. The model covers the entire Sequim Bay and surrounding intertidal wetlands with an unstructured mesh that has a spatial resolution varying from less than 10 m near the entrance channel to approximately 500 m at the open boundary. The open boundary conditions are forced with water level time series from the Salish Sea Model output. The model consists of roughly 32 000 elements and ten depth layers. Surface current routinely exceeds 2 m/s at the Sequim Bay entrance during peak flood and ebb (see Fig. 2), while the maximum can exceed 3 m/s during the peak spring tide. The flow model was used to predict tidal velocity for a 10-day period with 15-min resolution. A second model run generated 1-min resolution velocity data for an 8-h time period. The finely resolved data was needed to more accurately resolve model environmental conditions for a comparison with experimental validation testing.

This output, combined with bathymetry measurements from a 1.5 m resolution multibeam sonar survey, results in a spatiotemporal database of flow at the site over most of a neap-spring tidal cycle and drives the ASV and turbine dynamic simulations. Data are imported into the MATLAB-Simulink environment for the surface bin, as the ASV interacts with flow at the surface, and the tidal turbine is assumed to be suspended from a stationary surface platform. The model queries a scattered interpolant object [21] to retrieve the surface velocity vector at any spatial

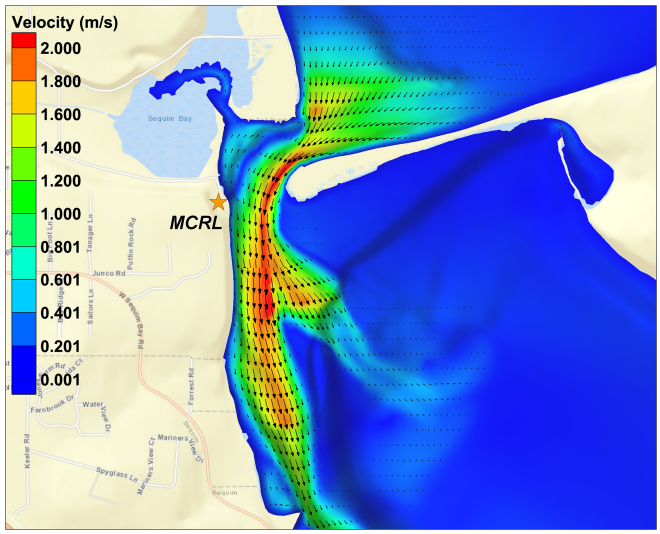

Fig. 2. Example snapshot of the surface current field at Sequim Bay entrance based on FVCOM-simulated velocity at July 29, 2022 22:30:00 GMT, which corresponds to the peak flood tide that day.

location within the simulation domain at the queried time. Linear interpolation is used to determine values falling between datapoints. To provide random variation between 15-min changes in the mean flow, we apply a simple turbulence model; 0%–10% of the mean, randomly selected, modifies flow velocity at each simulation timestep.

2) Mission Planning: ASVs typically move along preprogrammed paths during survey operation. In this model, a waypoint generation script is used to generate survey paths for the simulation within the boundaries of the fluid model domain. The script requires both the boundaries of the desired survey area as latitude/longitude coordinates defining the vertices of a polygon and the desired spacing between transects. Transect lines are determined based on the upper and lower limits of this polygon and the specified line spacing. The transect line segments are formatted for transition from one line to the next, (e.g., west–east movement to east–west movement) and then connected, resulting in a list of the vertices of the end points for each line. These vertices are interpolated based on the desired speed of the vehicle and total length of the path to produce a

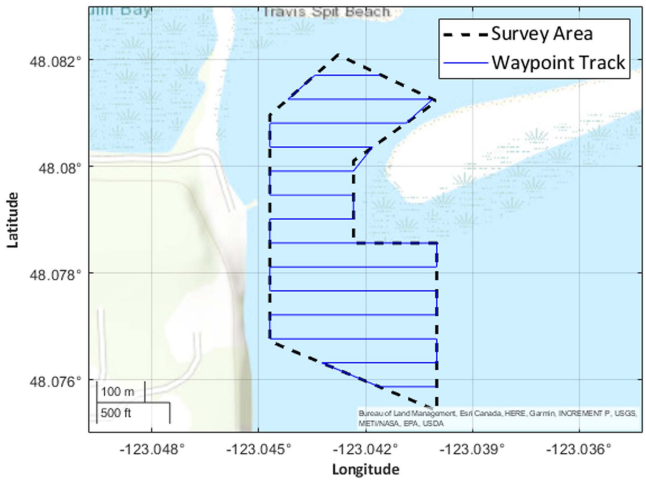

Fig. 3. Flow mapping survey area and transects (Sequim Bay).

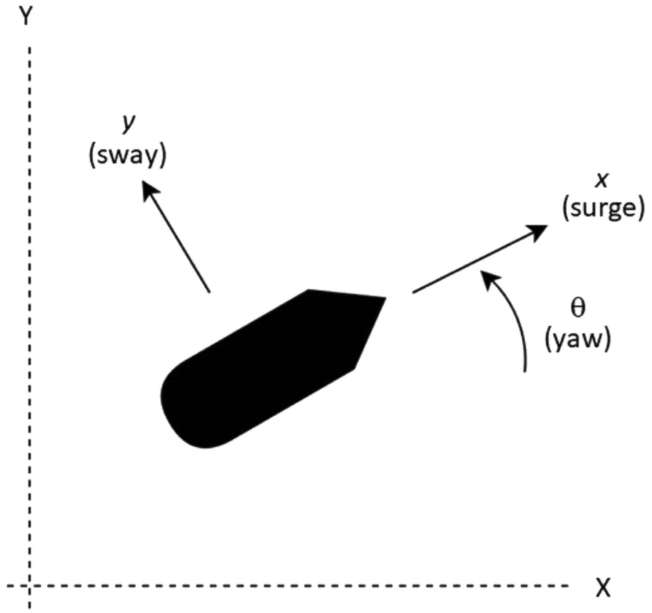

Fig. 4. Global and local coordinate system.

matrix containing target waypoints at smaller, regular intervals along the entire path. Coordinates are converted to Universal Transverse Mercator to match the format of the flow model. Fig. 3 depicts the output of this script for a representative survey that could use an ASV with tidal-powered recharging. This survey is designed to monitor tidal current speeds in the inlet of Sequim Bay. The flow mapping survey of our use case is composed with 50 m transect spacing, a vessel speed of 2.58 m/s, and encompasses an area of approximately 0.5 km^2 within the inlet of Sequim Bay.

The mission planning and control models in the present version of this tool do not consider obstacle avoidance. It is assumed that survey boundaries and target waypoints are set such that the resulting path does not present a collision risk to the vehicle.

3) ASV Motion: We model the ASV using a simplified horizontal vessel model [22] with three degrees of freedom: sway (port-starbird axis), surge (stern-bow axis), and yaw (rotational about the vertical heave axis) directions. The model considers forces and moments applied to the vessel by both propulsion and tidal currents (i.e., from the hydrodynamic flow model). Wind- and wave-induced forces are neglected because of a desire to minimize the complexity of the model (minimizing model runtime) and a lack of accessible realistic modeled data for wind and waves with the same fidelity as the tidal data supplied by PNNL's FVCOM model. Model inaccuracies caused by neglecting wind and waves will be minimal in calm sea-states, such as those typically found in Sequim Bay. The governing equations of motion are presented in the global coordinate frame (specifically, Y is north and X is east) in (1)–(3), and the associated variables are identified in the Nomenclature.

Forces applied by the vessel's thrusters and drag due to the vessel's movement through water may be used to calculate resulting linear acceleration in the global coordinate frame using

$$m\dot{v}_{\text{asv}} = \begin{bmatrix} \cos\theta_{\text{asv}} \\ \sin\theta_{\text{asv}} \end{bmatrix} T + F_D\left(\theta_{\text{asv}}, v_{\text{asv}}, v_{\text{curr}}\left(x_{\text{asv}}\right)\right) \quad (1)$$

where $F_D(\theta_{\text{asv}}, v_{\text{asv}}, v_{\text{curr}}(x_{\text{asv}}))$ is the force of drag on the ASV considering ASV orientation (θ_{asv}), velocity (v_{asv}), and water velocity (v_{curr}), and the overdot on v_{asv} indicates a time-derivative. The drag force is most easily and naturally defined in a local reference frame, so we will forego specifying its exact form until after the necessary coordinate transformations have been performed. Thrust force T is a scalar quantity in the direction of ASV orientation, and for the purpose of modeling linear dynamics, we treat the ASV as a point mass with an added mass term included in m to account for additional inertia caused by accelerating fluid around the vessel.

The effect of these forces on vessel rotational acceleration is included as

$$I_z\dot{\omega}_{\text{asv}} = \tau + F_{D,\tau}(\omega_{\text{asv}} - \nabla \times v_{\text{curr}}(x_{\text{asv}})) \quad (2)$$

where τ represents torque due to ASV thrusters, $F_{D\tau}$ is torque caused by rotational drag, and I_z is ASV moment of inertia about the heave axis. Inertial added mass is neglected. Rotational drag ($F_{D,\tau}$) is calculated considering vessel angular velocity and drag coefficient $C_{D,\tau} = 0.15$ kg/m^2

$$F_{D,\tau}(\omega_{\text{asv}}) = -C_{D,\tau}\text{sgn}\left(\omega_{\text{asv}}\right)\omega_{\text{asv}}^2. \quad (3)$$

These kinematics are transformed into a local reference frame where the "x"-axis is aligned with the surge direction of the ASV and the "y"-axis is aligned with the sway direction of the ASV (see Fig. 4).

Current is assumed to be irrotational, and thus the rotational dynamics remain the same as in the global frame. The linear dynamics are put through a coordinate transformation

$$\tilde{v}_{\text{asv}} = \begin{bmatrix} \cos\theta_{\text{asv}} & \sin\theta_{\text{asv}} \\ -\sin\theta_{\text{asv}} & \cos\theta_{\text{asv}} \end{bmatrix} v_{\text{asv}}$$

$$\Rightarrow v_{\text{asv}} = \begin{bmatrix} \cos\theta_{\text{asv}} & -\sin\theta_{\text{asv}} \\ \sin\theta_{\text{asv}} & \cos\theta_{\text{asv}} \end{bmatrix} \tilde{v}_{\text{asv}}. \quad (4)$$

The transform results in velocity vector $\tilde{v}_{\text{asv}}$ representing vessel velocity in the surge and sway directions, which is presented in (4) in matrix form. Vessel acceleration in the surge and sway directions ($\dot{\tilde{v}}_{\text{asv}}$) is calculated as the derivative of $\tilde{v}_{\text{asv}}$ as follows:

$$\begin{aligned}\dot{\tilde{v}}_{\text{asv}} &= \frac{d}{dt}\left(\begin{bmatrix}\cos\theta_{\text{asv}} & \sin\theta_{\text{asv}}\\ -\sin\theta_{\text{asv}} & \cos\theta_{\text{asv}}\end{bmatrix} v_{\text{asv}}\right)\\ &= \omega_{\text{asv}}\begin{bmatrix}-\sin\theta_{\text{asv}} & \cos\theta_{\text{asv}}\\ -\cos\theta_{\text{asv}} & -\sin\theta_{\text{asv}}\end{bmatrix} v_{\text{asv}}\\ &\quad + \begin{bmatrix}\cos\theta_{\text{asv}} & \sin\theta_{\text{asv}}\\ -\sin\theta_{\text{asv}} & \cos\theta_{\text{asv}}\end{bmatrix}\dot{v}_{\text{asv}}. \end{aligned} \tag{5}$$

The resulting acceleration in surge and sway consists of two terms: an implicitly produced Coriolis term dependent on vessel rotational speed ω_{asv}, and an x–y acceleration term transformed to the surge–sway direction with the same coordinate transform as in (4). The Coriolis term is attributed to the rotation of the local reference frame with respect to the global inertial reference frame.

Furthermore, in the local coordinate frame, we can naturally define the force of drag as

$$\tilde{F}_D(v) = \begin{bmatrix}-C_{D,x}\,\text{sgn}\,(v_x)\,v_x^2\\ -C_{D,y}\,\text{sgn}\,(v_y)\,v_y^2\end{bmatrix} \tag{6}$$

$$v \equiv \tilde{v}_{\text{asv}} - \begin{bmatrix}\cos\theta_{\text{asv}} & \sin\theta_{\text{asv}}\\ -\sin\theta_{\text{asv}} & \cos\theta_{\text{asv}}\end{bmatrix} v_{\text{curr}}\,(x_{\text{asv}}) \tag{7}$$

where v_x and v_y refer to the surge (x) and sway (y) components of v, respectively. Note that the drag force coefficients $C_{D,x}$ and $C_{D,y}$ are different for the surge and sway directions, as they include vessel drag coefficient, cross-sectional area perpendicular to flow, and fluid density. In terms of drag force in the global coordinates, F_D, we have

$$\begin{aligned}&\tilde{F}_D\left(\tilde{v}_{\text{asv}} - \begin{bmatrix}\cos\theta_{\text{asv}} & \sin\theta_{\text{asv}}\\ -\sin\theta_{\text{asv}} & \cos\theta_{\text{asv}}\end{bmatrix} v_{\text{curr}}\,(x_{\text{asv}})\right)\\ &= \begin{bmatrix}\cos\theta_{\text{asv}} & \sin\theta_{\text{asv}}\\ -\sin\theta_{\text{asv}} & \cos\theta_{\text{asv}}\end{bmatrix} F_D\left(\theta_{\text{asv}}, v_{\text{asv}}, v_{\text{curr}}\,(x_{\text{asv}})\right). \end{aligned} \tag{8}$$

Using the definition of vessel velocity in global coordinates defined in (1), the full equation of linear motion in surge–sway coordinates results in

$$\begin{aligned}\dot{\tilde{v}}_{\text{asv}} &= \omega_{\text{asv}}\begin{bmatrix}0 & 1\\ -1 & 0\end{bmatrix}\tilde{v}_{\text{asv}} + \frac{1}{m}\begin{bmatrix}T\\ 0\end{bmatrix}\\ &\quad - \frac{1}{m}\tilde{F}_D\left(\tilde{v}_{\text{asv}} - \begin{bmatrix}\cos\theta_{\text{asv}} & \sin\theta_{\text{asv}}\\ -\sin\theta_{\text{asv}} & \cos\theta_{\text{asv}}\end{bmatrix} v_{\text{curr}(x_{\text{asv}})}\right). \end{aligned} \tag{9}$$

The terms are, in order, Coriolis force due to the rotation of the local surge–sway reference frame relative to the global x–y reference frame, thruster force acting only in the surge direction, and drag force in the surge–sway reference frame due to relative ASV velocity. The flow model described in Section II-A-1 provides water velocity, and a control block designs thrust and torque using proportional–integral (PI) force and angular orientation controllers (described in Section II-A-4).

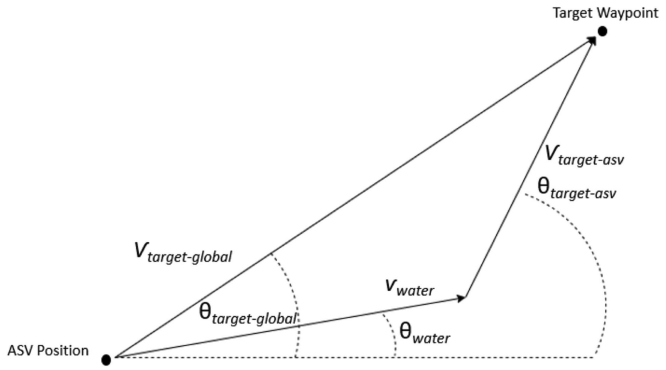

Fig. 5. Velocity vectors described in (10).

4) ASV Control Design: The ASV control block contains two separate controllers: a PI controller commanding thrust, and a proportional–integral–derivative (PID) controller commanding torque provided by the ASV's propellers. The thrust controller omits a derivative component to minimize instantaneous changes in force. However, a derivative component implemented in the torque controller minimizes oscillations that were otherwise present in vessel heading without creating instability in the controller. Global velocity and heading errors feed the thrust and torque controllers, respectively.

The torque controller takes inputs of instantaneous ASV heading, position in the simulation domain, ASV actual and target velocity, water velocity, and target waypoint from the path planning model. The controller calculates target heading while considering the speed and direction of water velocity, as well as the actual speed of the ASV relative to water. Fig. 5 depicts this relationship, presented in (10), where $\theta_{\text{target}-\text{asv}}$ is the target vessel heading, $v_{\text{target}-\text{global}}$ and $\theta_{\text{target}-\text{global}}$ represent target ASV velocity over ground, and the water velocity vector consists of v_{water} and θ_{water}

$$\theta_{\text{target}-\text{asv}} = \arctan\frac{v_{\text{target–global}}\sin\theta_{\text{target–global}} - v_{\text{water}}\sin\theta_{\text{water}}}{v_{\text{target}-\text{global}}\cos\theta_{\text{target}-\text{global}} - v_{\text{water}}\cos\theta_{\text{water}}}. \tag{10}$$

The target heading, $\theta_{\text{target}-\text{asv}}$, is used with the instantaneous ASV heading to calculate the heading error fed into the PI torque controller. We set controller gains using a step-and-settle method [23], by which a constant target heading setpoint was applied and PID values were adjusted to minimize oscillations and steady-state error in resulting ASV heading.

The thrust controller takes inputs of target velocity and instantaneous ASV velocity to generate force in the surge direction through the propellers. Commanded velocity has a ramp and settle shape with a slope of 1 m/s^2 and maximum speed of 2.58 m/s—the maximum achievable speed of the ASV used in experimental testing. Target velocity decreases to half maximum speed when the ASV rounds corners.

We again set controller gains using a step-and-settle method. For both heading and velocity tuning, we identified target accuracy as a relative error of $<5\%$. Table I summarizes tuning results, including steady-state relative error and settling time for both velocity and heading controllers.

TABLE I
CONTROLLER TUNING RESULTS

	P	I	D	Settling time (s)	Steady-state relative error
Velocity	2000	700	0	3	0.0036
Heading	700	50	50	25	0.0014

Heading settling time is comparable to settling times of model-free adaptive control [24] and PID control in existing work [25], though methods with faster settling times have been demonstrated using a state error port-controlled Hamiltonian approach [26]. These combinations of settling time and steady-state error provide acceptable control over vessel heading and velocity for this model's purpose.

Note that the simulation assumes commanded torque and thrust are identical to the resulting torque and thrust applied to the vessel. A higher fidelity model would include electromechanical models of the vessel's propellers and motors, with additional PID loops to control resulting torque and thrust based on commanded values. This model design seeks to maximize accuracy while minimizing complexity, so the additional complexity was foregone in favor of lower simulation runtimes with adequate accuracy.

5) ASV Battery Model: The model implements energy storage aboard the ASV using Simulink's built-in battery block; the propeller thrust force, vessel velocity, and representative efficiencies of power components are used to determine a current draw from the battery. The mechanical power resulting in ASV velocity is the product of vessel velocity and thruster force. The model assumes efficiencies of 88%, 88.5%, and 75% due to battery, motor, and thruster inefficiencies, respectively, resulting in electrical power from the vessel battery. Current draw is then

$$I_{\text{bat}} = \frac{s_{\text{asv}} T}{V_{\text{bat}} \eta} \tag{11}$$

where s_{asv} is the ASV's relative speed in the local coordinate frame, T is thruster force applied to the vessel, V_{bat} is battery voltage, and η is cumulative efficiency of the ASV's battery, motor, and thrusters. Current draw from the battery is used to update the battery's state of charge.

6) Turbine Model: This model subsystem simulates a cross-flow tidal turbine serving as the energy-harvesting device for our case study. This is built on a turbine model initially designed to analyze tidal energy system efficiency, with a detailed description of turbine dynamics presented by Hanif et al. [27]. The subsystem receives tidal velocity at the turbine location as an input and outputs torque and rotation rate on the turbine shaft resulting from an implemented maximum power-point tracking (MPPT) controller as an output. This model is stable for most input velocity conditions except where the turbine should stall (rotation rate reaches zero due to drop in inflow velocity). To improve stability and similarity to an actual implementation, we add a cut-in speed nonlinear controller. During actual turbine operation, the rotor would not operate under a minimum velocity. We accomplish this using a conditional "if-action" sequence that checks the inflow velocity and either passes the value to the next simulation step or zeros out speed and torque outputs. Once inflow speed is sufficiently high for operation, the turbine accelerates from rest. The rotor's inertia prevents it from having rapid stop-start events. However, at this time we have not implemented a realistic speed deceleration when the speed drops below cut-in. Although unrealistic, this does not greatly affect turbine power output performance.

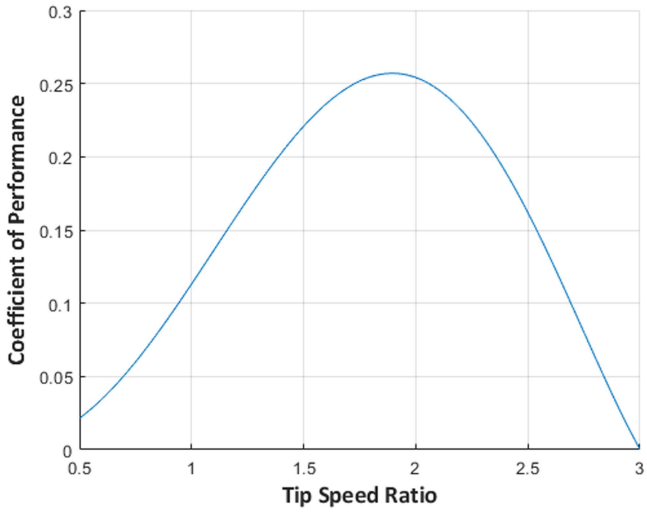

Fig. 6. Coefficient of performance as a function of tip-speed ratio.

TABLE II
TURBINE PROPERTIES

Property	Value	Units
Diameter	1	m
Height	1	m
Moment of Inertia	8.05	kg-m^2
Rated power	600	W
Cut-in speed	0.6	m/s

The turbine's characteristic performance is described by Bachant and Wosnik [28]. A polynomial fit for the coefficient of performance as a function of tip speed ratio $C_P(\text{TSR})$, depicted in Fig. 6, determines conditions representing peak performance for MPPT control. Additional turbine properties can be found in Table II. The turbine is simulated in a location within the Sequim Bay velocity dataset that features a high surface current and proximity to the MCRL facility. Specifically, the simulated turbine is located at 48.08 and -123.04 latitude and longitude, respectively.

7) Generator Model: A generator and battery model represents the conversion of mechanical energy harvested by the turbine to electrical energy. The generator module receives the speed of the turbine and commanded torque from the turbine model. Torque represents the needed load, produced by the

TABLE III
PMSM PROPERTIES

Property	Value	Units
Stator phase resistance	0.04	Ω
Armature inductance	0.00095	H
Flux linkage	0.2651	Vs
Moment of inertia	4.851	kg-m^2
Pole pairs	5	

Fig. 7. PNNL's ASV Jonesy.

generator, on the turbine to maintain its peak efficiency and regulate its speed. The model uses Simulink's built-in permanent magnet synchronous machine (PMSM) and battery models with parameters selected to achieve power output based on the modeled turbine's 600 W rated power. The battery is nominally 66 kWh and generator parameters can be found in Table III.

A field-oriented control methodology [29] regulates current at the terminals to achieve torque at the generator shaft. The model uses a bidirectional inverter to convert three-phase power from the generator to direct current (dc) and a dc/dc converter to reduce voltage to a suitable level for the battery (24 V nominal). The simulation tracks the battery's state of charge as power input from the turbine model is fed through the electrical subsystem.

B. Experimental Validation

We deployed the ASV modeled in this simulation in Sequim Bay, WA on July 7, 2022 and programmed it to move through several survey patterns, acceleration, and free decay testing maneuvers to collect data used in defining the simulation parameters. Experimental validation aimed to identify accurate added mass and drag coefficients for the vehicle.

1) Autonomous Surface Vehicle: We consider PNNL's ASV Jonesy, an SR Utility 3.0 model produced by SeaRobotics (see Fig. 7), for our use case and experimental validation. Table IV lists a selection of physical characteristics specific to this ASV. Moment of inertia refers to inertia with respect to the heave (vertical) axis from a CAD model provided by SeaRobotics.

The ASV may be equipped with a variety of sensors to support varied operations. During this deployment, we collected data

TABLE IV
ASV JONESY PROPERTIES

Property	Magnitude	Units
Mass	335.4	kg
Moment of inertia	280.1	kg-m^2
Length	3	m
Beam	2	m
Draft	0.42	m
Drag coefficient	0.6149	Unitless
Added mass coefficient	1.4	Unitless

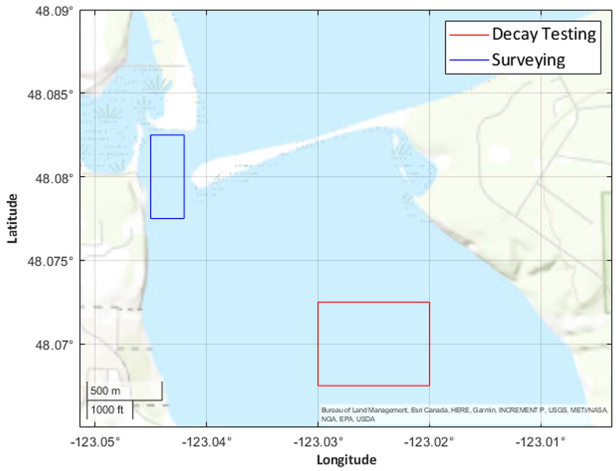

Fig. 8. Locations of validation testing.

including position and heading from an Advanced Navigation GNSS Compass, speed over ground, power draw, and battery state of charge. Additionally, the ASV carried a Nortek Signature 1000 VM acoustic Doppler current profiler (ADCP) measuring water velocity requisite for a flow mapping use case, a Xylem EXO2 water quality sensor, a Lishen C16 LiDAR for obstacle detection, an AIS transponder, and an Airmar DT800 depth sounder. We guided the ASV through two sets of maneuvers to obtain measurements for model validation and refinement. The first test involved a series of acceleration and decay maneuvers intended to identify drag and added mass coefficients. For this testing, we manually maneuvered the ASV to a calm (i.e., low wind and current) area in Sequim Bay, depicted in Fig. 8.

In a first stage of field testing, we directed the ASV to move south and brought it up to maximum speed by manually commanding 100% thrust. The vessel maintained constant maximum speed for approximately 30 s before power was cut and it naturally drifted to a stop. We repeated this test with varying levels of thrust and and then again while directing the ASV to move north. Table V identifies these tests.

The ASV performed a second set of maneuvers in the faster-moving Sequim Bay channel. It moved through a series of cross-channel transects typical of a flow mapping survey. While the ASV was able to complete the survey, the vessel overshot its first target waypoint and required manual intervention to avoid running aground.

TABLE V
ACCELERATION AND DECAY TESTING

Test identifier	Thrust [% of Maximum]	Direction
1	15	South
2	30	South
3	45	South
4	60	South
5	75	South
6	100	South
7	15	North
8	30	North
9	45	North
10	60	North
11	75	North
12	100	North

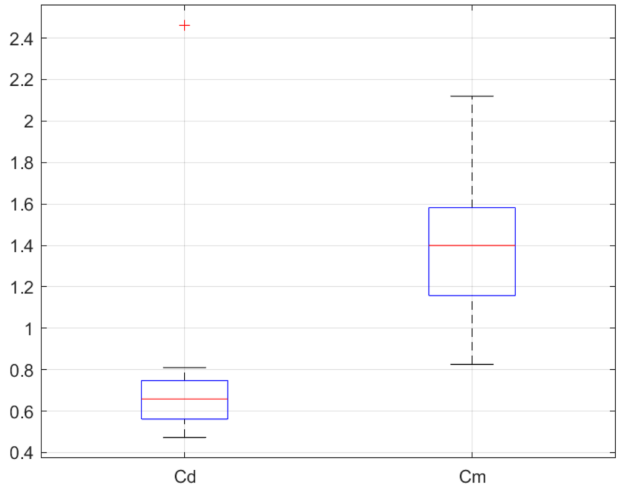

Fig. 9. Boxplots presenting calculated drag and added mass coefficients.

C. Model Refinement

We analyzed data collected during the validation deployment and used the results to refine the simulation to more accurately reflect the dynamics and power consumption of the ASV. This resulted in the calculation of a drag coefficient and an added mass coefficient from experimental data.

1) Drag Coefficient Calculation: We determined an approximate drag coefficient for the ASV by analyzing acceleration and decay testing data by individual test iteration (see Table V), calculating surge-direction drag coefficients, and averaging the results. Efficiencies of 88%, 89%, and 75% were applied to account for battery, motor, and thruster/propeller power losses, respectively. These values were based on specification sheets for the components on ASV Jonesy and reasonable representative ranges of respective component efficiencies. Mechanical power P is defined as the product of ASV relative velocity and force while the ASV traveled at constant speed, and it is related to power recorded at the battery (P_{bat}) through battery, motor, and thruster efficiency η as shown in (13)

$$P = s_{\text{asv}} F_D \tag{12}$$

$$P = \eta P_{\text{bat}}. \tag{13}$$

Under this condition, and neglecting the effects of wind and waves, it is assumed that vessel thrust is balanced by vessel drag, and thus the drag coefficient can be calculated by

$$C_D = \frac{2P_{\text{bat}}\eta}{\rho A s_{\text{asv}}^3} \tag{14}$$

where s_{asv} is the ASV's speed relative to water, A is ASV cross-sectional area in the surge direction, and η represents combined battery, motor, and thruster efficiency. Using measured salinity recorded by sensors in Sequim Bay, we determined water density ρ to be 1012 kg/m^3.

We averaged water velocity recorded by the ADCP over the upper meter of available data to determine surface water velocity. ADCP data during ASV movement were unreliable, possibly due to interference from entrained air or cavitation bubbles from propeller operation. Instead, we averaged water velocity data collected over the minute before movement to determine vessel relative velocity during movement. Because testing occurred near slack tide, relative velocity is dominated by vessel velocity rather than water velocity, so errors due to the assumption of temporally constant water velocity are minimal.

By taking an average of the results from tests performed in opposite directions, the ASV's drag coefficient can be reasonably approximated to be 0.61. The multiple tests and opposing directions of movement were intended to negate external disturbances, such as wind or variations in water velocity. In addition, the lowest percent thrust tests (1 and 7) demonstrated a trend of larger calculated drag coefficients relative to the other tests in each respective direction of testing. Test 1 resulted in a calculated drag coefficient of 0.7, 15% greater than the average southbound test, and test 7 produced a drag coefficient of 2.5, or 310% above the average northbound test. This is potentially due to a larger contribution of wind forces to ASV velocity at lower vessel speeds (relative to contributions by propulsion and drag forces) or due to the lack of instantaneous ADCP data during movement. Efficiency may drop at lower power levels, and because efficiencies in this model are assumed to be static, this effect also influences a changing calculated drag coefficient. Fig. 9 uses boxplots to depict results for both the drag coefficient and the added mass coefficient calculations presented in Section II-C-2. The outlier depicted (test 7, 15% thrust north) was omitted from final drag coefficient calculations due to its value beyond the reasonable range of drag coefficients for common bodies [30].

2) Added Mass Coefficient: We performed similar calculations using the acceleration and decay tests to identify an added mass coefficient representing the added mass (C_m) of the accelerated water entrained by the ASV. Assuming only drag force acted on the ASV as it slowed during free decay maneuvers, balance is achieved between fluid and inertial forcing such that

$$F_{\text{hyd}} = m\dot{v}_{\text{asv}}$$

$$F_D + F_{Cm} = m\dot{v}_{\text{asv}} \tag{15}$$

where m is the mass of the ASV, v_{asv} is a polynomial fit to the ASV velocity after a moving average smoothing function with

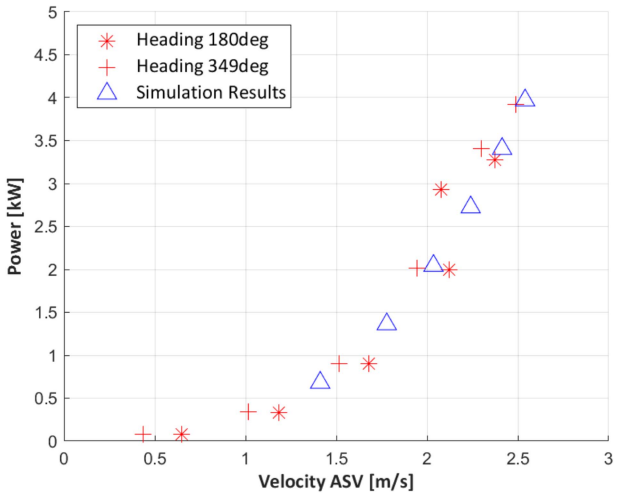

Fig. 10. ASV thruster power draw versus velocity for experimental and simulation testing.

a window size of 10 s was applied, and $\dot{v}_{\text{asv}}$ is the derivative of the velocity polynomial. For each test, a window was chosen beginning with the moment ASV velocity starts to decrease, and ending when ASV acceleration reaches zero, signaling the end of deceleration. The hydrodynamic force, F_{hyd}, is composed of drag acting on the ASV, F_D, and an added mass force, F_{Cm} [31]. The additional weight due to accelerating water around the ASV, M, can then be isolated and used to calculate the added mass coefficient C_m

$$M = m - \frac{F_D}{\dot{v}_{\text{asv}}} \tag{16}$$

$$M = \rho V_{\text{asv}} C_m \tag{17}$$

$$C_m = \frac{m - \frac{F_D}{\dot{v}_{\text{asv}}}}{\rho V_{\text{asv}}} \tag{18}$$

where V_{asv} is the volume of the ASV underwater, and ρ is the density of seawater. We used a least-squares regression to correlate drag force and acceleration over the chosen window. Fig. 9 depicts the results of these calculations, which produced an average added mass coefficient across all experimental test iterations of 1.4.

III. Results

A. Validation Results

After identification and implementation of the hydrodynamic coefficients determined in Section II-C, we ran the Simulink model for full thrust testing in the north and south directions. Parameters included input water velocities recorded by the ADCP (0.02 m/s W and 0.06 m/s S) and a target vessel velocity of 2.58 m/s based on maximum velocity observed in empirical data. Results from the simulation determined maximum thrust force, and then we simulated the remaining decay tests (<100% thrust scenarios). We compared outputs with empirical data and calculated percent error.

TABLE VI
Simulation Error

	North	South
Velocity error	5.7%	4.3%
Velocity rise time error	7.3%	35.3%
Power draw error	14%	3.5%
Power draw rise time error	33.8%	3.4%

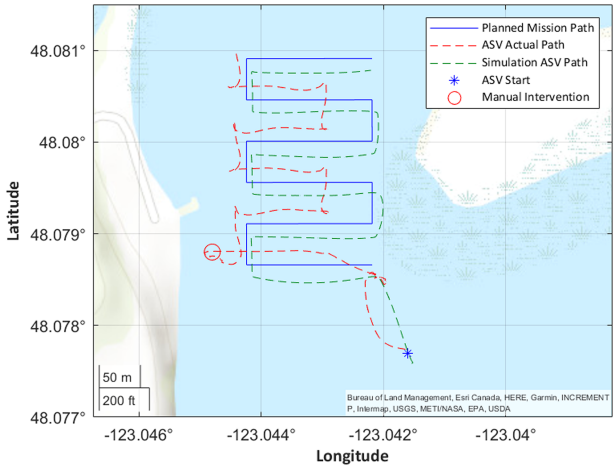

Fig. 11. Actual and simulated survey path results.

Fig. 10 presents the results for ASV power consumption and velocity for each experimental test and the corresponding simulations. Agreement between simulated and experimental results reflects the expected cubic relationship between velocity and power.

Table VI lists simulation errors encountered during further investigation of simulated vessel velocity and power draw for full thrust testing scenarios. Data demonstrate that the model with appropriate input parameters and experimentally-derived drag and added mass coefficients produces accurate vessel velocity and power draw profiles. Velocity error compares maximum empirical velocity at full thrust with simulated data for both north and south testing, and power draw error is compared for the same scenario. Rise time error for both variables is a comparison of the rate of increase in velocity and power draw, respectively, during acceleration using linear regression fits to empirical and simulated data.

Increased rise time errors (i.e., above 30%) may be influenced by the low number of data points collected during acceleration (constant velocity was reached after only a few seconds, and data were collected at a frequency of 1 Hz), or due to potential environmental disturbances like wind during testing. Velocity errors within approximately 5% were considered acceptable.

Next, the FVCOM tidal velocity model described in Section II-A-1 generated a dataset of simulated tidal velocities for the time period of experimental testing in order to evaluate the performance of the ASV model in a realistic survey scenario including significant tidal current. Fig. 11 depicts the ASV's commanded, actual, and simulated position within the survey domain.

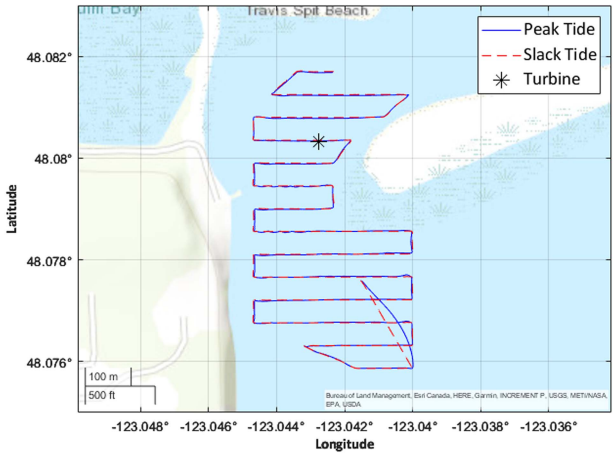

Fig. 12. Peak flow and slack tide survey path results.

TABLE VII
ENERGY CONSUMED FOR VARYING TIDAL SCENARIOS AND COMMANDED ASV VELOCITIES

	Power consumed	Survey time
$v_{\text{asv}} = 2.58m/s$, Peak Flow	2.1 kWh	30.4 min
$v_{\text{asv}} = 2.58m/s$, Slack Tide	1.9 kWh	30.6 min
$v_{\text{asv}} = 1.5m/s$, Peak Flow	2.2 kWh	73.7 min
$v_{\text{asv}} = 1.5m/s$, Slack Tide	716 Wh	50.2 min

Overall the simulation exhibited superior waypoint tracking ability as compared to field testing. This can be explained in part by site conditions that are more complex than can be represented in simulation. However, suboptimal behavior due to the physical ASV's control strategy during field trials is evident as the ASV consistently overshoots waypoints and must correct. This is particularly noticeable at the first corner where manual intervention was required to keep the ASV on track during experimental testing. In contrast, the simulation accounts for future waypoints and turns, and it adjusts speed accordingly.

B. Full Use Case Simulation

After model refinement and validation, we performed a full use case simulation of colocated ASV survey operation and tidal turbine energy harvesting. The survey consisted of horizontal transects of 50 m separation distance, and the simulation modeled both slack (low water velocity) and peak (high water velocity) flow scenarios. Each modeled tidal condition occurred at flood tide to ensure consistency between the direction of water movement for accurate comparison. Fig. 12 shows the ASV's position trace through the simulation domain.

The FVCOM model provided an existing dataset of input water velocities for dates between October 1, 2017 and October 10, 2017. Water velocities reached a maximum of 1.41 m/s during peak flow, though the maximum possible for this location can reach up to 2.5 m/s. Fig. 13 depicts the magnitude of water velocity recorded at the ASV's location in each simulated survey.

Table VII lists power consumption and survey time for the two environmental conditions. Total power consumption was slightly higher during peak flow conditions, mostly due to the increased length of time required to complete the survey. Slack tide power consumption of 1.9 kWh constitutes 25.6% of total ASV battery storage. As a demonstration of the simulation's utility for mission planning, we iterated survey speed to explore its impact on energy use. Decreasing the target survey speed to 1.5 m/s decreased energy consumption during simulated slack tide but increased it during peak flow. Survey completion time increased for both tidal scenarios. Energy consumption during peak flow conditions with low target vessel velocity is high because of 25 min in the middle of the channel where the simulated vessel struggled to make headway against currents matching its target speed.

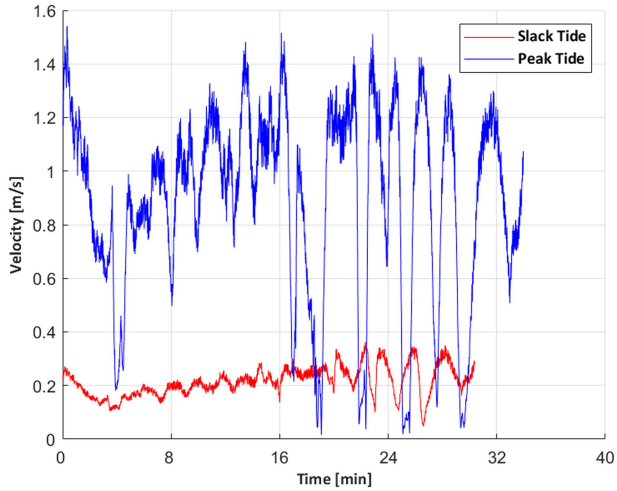

Fig. 13. Peak and slack tide water velocities.

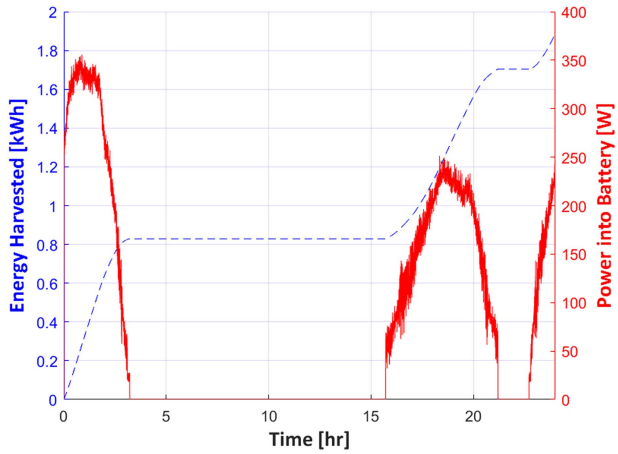

Fig. 14. Tidal turbine power generated and total energy accumulated.

The modeled tidal turbine harvested 1.9 kWh of power during the simulation period (see Fig. 14). Noise was present in the generator system on the order of ± 10 W of the mean power measured at the battery. Increasing the electrical components' switching frequency from 1 to 10 kHz in simulation reduced noise to the scale of 1 W. However, such a high switching frequency also led to unsustainable simulation runtimes. Instead, we applied a low-pass filter to reduce noise in the generator system while maintaining feasible simulation runtimes.

IV. Discussion

Simulation results for the varying environmental conditions and target survey speeds presented in Section III demonstrate the ability of the ASV to successfully navigate missions in high-flow areas, such as in Sequim Bay channel, and support the feasibility of sustaining operations with energy harvested by a colocated tidal turbine. Results indicate the ability of the modeled turbine to power up to 2 ASV survey missions per day at lower target survey speeds and calm environmental conditions. The model may be used to iterate survey, vessel, and turbine design parameters to achieve required or desired performance. Similarly, while this method is only shown for a Sequim Bay location, simulation of this use case can be performed in any domain for which spatiotemporally-resolved water velocity information is available. This method is most appropriate for zones where current (e.g., river, tidally-driven, or ocean) is likely to be the major driver of environmental loading.

We considered model validation successful with steady-state ASV velocity errors of 4%–6% and power consumption errors of 3%–14%. Increased error (up to 30%) in velocity and power consumption during transient vessel acceleration is acceptable because the surveying maneuvers analyzed here spent significantly more time at constant velocity than they spent accelerating and decelerating. Error is attributable to systematic and random uncertainty in measured ASV performance indicators and environmental parameters (e.g., thruster power and water velocity, respectively). In addition, error influenced by the model's lack of consideration of wind and wave effects, though limited due to care in experimental work, is still apparent. Impacts can be observed in the experimentally derived drag coefficients because those determined in southward testing were lower than those in northward testing. This can be explained by the presence of a southern wind. Performance of the system will vary with operating conditions, as harsher wind and wave conditions require more power from the ASV to navigate, and some sea states may be too harsh to operate in. For example, the system used in this testing is capable of operating in up to Beaufort [32] force 3 wind/waves. If wind and wave effects were to be added to this model, wave field and wind speed datasets similar to the spatiotemporally resolved water velocity data could be used. In addition, simulated water velocity driving the model is of lower temporal resolution (1 min) than measured quantities during field trials and is decoupled from other simulation components. This results in a condition in which flow has an effect on the turbine and vessel, but the latter return no effect back on the flow. For small turbines and ASVs, it is a reasonable assumption that impact on the flow would be minimal, but for larger turbines or arrays or larger vessels, neglecting impact on the flow field would be problematic.

The ADCP used during field trials struggled to collect reliable water velocity measurements at depth during movement, possibly due to air bubbles moving underneath the vehicle, or due to few particles moving in the water at slack tide. A lack of instantaneous flow data during validation testing leaves room for error in accurately determining the ASV's hydrodynamic coefficients. We predict this error to be small because the testing was conducted near slack tide—when water velocity before and during testing should have been consistently low.

Differences are apparent between the simulated ASV track and its motion during field trials of a survey mission in the tidal channel. This variation can be explained by the different control schemes used in the ASV model and the actual ASV Jonesy. The simulation has access to more input information on which to base decisions, such as instantaneous (and to the model, "true") water velocity, that are considered when adjusting propulsion force and torque. ASV Jonesy does not currently include this in decision-making, though ADCP data would provide a real-time estimate of local flow speed. Similarly, ASV Jonesy's waypoint tracking controller was operating with preset gains and lacked turn approach speed adjustment. The "black box" nature of the real vehicle's control scheme makes direct comparison of complex movement challenging; our validation focused on acceleration and decay testing where ASV inputs could remain constant between modeled and actual experimental conditions. Future efforts will work to align control methodologies between the digital and physical platforms.

We initially constructed the model in smaller subsystems that were run independently (i.e., the turbine model was run separately from the ASV motion and control models). Subdivision of the simulation components was necessitated by high complexity of individual components, the variety of electrical and mechanical processes modeled, and the large numbers of inputs. We integrated these individual components into a single model, consisting of combined tidal turbine, generator, ASV motion, and control blocks; however, the simulation remains computationally expensive. The described version has a runtime of approximately three times the simulated time, which presents a problem for simulations of extended duration. Improvements could be made by considering other coding environments and data formats. In addition, the model currently relies on inputs from PNNL's FVCOM model or tidal velocity data of similar format and resolution, which contributes to slower runtimes because the dataset is quite large and is queried at each time step.

Future work will explore migrating the tool to alternate coding environments and increasing computational efficiency of the model. In addition, the model may be adapted to accept robot operating system commands in order to provide feedback for control algorithm testing.

V. Conclusion

The results of this effort demonstrate the ability of in situ energy harvesting to support a particular ocean observation mission performed by an ASV. Tidal energy harvesting in the simulated location extends mission duration by removing the constraint of limited onboard energy storage and eliminates the need to return to shore for recharge. With proper autonomy and maintenance, a recharge node such as the one considered in this work has the potential to increase the availability of ocean observation data by removing restrictions imposed by a human operator not only in surveying, but in maneuvering and

recovering a vessel for recharge. Even so, limitations on the frequency and duration of missions remain and are dependent on resource availability, environmental conditions, and autonomous platform energy needs, which are site- and mission-specific. Simulation tools such as the one described in this work assist in understanding and designing technologies like the modeled recharge node powered by marine energy; however, challenges exist such as computation cost and the limited availability of data to inform such models. While this tool accurately simulates vessel dynamics and power consumption, the electromechanical systems modeled are computationally expensive in the chosen MATLAB-Simulink environment, and the model's reliance on spatially and temporally resolved water velocity data limits its applicability to mission sites where such information exists.

ACKNOWLEDGMENT

The authors would like to thank Erin Walters, Ted Nowak, Alex Turpin, and William Nelson for assistance with deployment and field trials in Sequim Bay. The views expressed herein do not necessarily represent the views of the DOE or the U.S. Government. The U.S. Government retains and the publisher, by accepting the article for publication, acknowledges that the U.S. Government retains a nonexclusive, paid-up, irrevocable, worldwide license to publish or reproduce the published form of this work, or allow others to do so, for U.S. Government purposes.

REFERENCES

[1] M. A. Moline et al., "Remote environmental monitoring units: An autonomous vehicle for characterizing coastal environments," *J. Atmos. Ocean. Technol.*, vol. 22, no. 11, pp. 1797–1808, 2005.

[2] J. Nash et al., "Autonomous CTD profiling from the robotic oceanographic surface sampler," *Oceanogr.: Official Mag. Oceanogr. Soc.*, vol. 30, no. 2, pp. 110–112, 2017.

[3] P. Kimball et al., "The WHOI Jetyak: An autonomous surface vehicle for oceanographic research in shallow or dangerous waters," in *Proc. 2014 IEEE/OES Auton. Underwater Veh.*, 2014, pp. 1–7.

[4] H. Oh, S. Kim, A. Tsourdos, and A. Savvaris, "Comparison of station keeping strategies for long endurance autonomous surface vehicle," *J. Mar. Sci. Technol.*, vol. 25, pp. 13–25, 2020.

[5] B. Liu, Y. Yang, S. Wang, and Y. Liu, "A dual-modal unmanned vehicle propelled by marine energy: Design, stability analysis and sea trial," *Ocean Eng.*, vol. 247, 2022, Art. no. 110702. [Online]. Available: https://www.sciencedirect.com/science/article/pii/S0029801822001548

[6] J. Bowker, M. Tan, and N. Townsend, "An autonomous vehicle concept capable of operating throughout the ocean space: Air, surface and subsea," *Proc. Inst. Mech. Eng., Part M: J. Eng. Maritime Environ.*, vol. 237, no. 4, pp. 918–928, 2023. [Online]. Available: https://journals.sagepub.com/doi/full/10.1177/14750902221150285

[7] Y. Yang and E. Martinez, "Feasibility analysis of a wave powered autonomous underwater vehicle," *Energy Convers. Manage.: X*, vol. 18, 2023, Art. no. 100352. [Online]. Available: https://www.sciencedirect.com/science/article/pii/S2590174523000089

[8] H. Li et al., "An extended-range wave-powered autonomous underwater vehicle applied to underwater wireless sensor networks," *iScience*, vol. 25, no. 8, 2022, Art. no. 104738. [Online]. Available: https://www.sciencedirect.com/science/article/pii/S2589004222010100

[9] R. Hine and P. McGillivary, "Wave powered autonomous surface vessels as components of ocean observing systems," in *Proc. PACON*, 2007, pp. 305–326.

[10] C. Meinig, N. Lawrence-Slavas, R. Jenkins, and H. M. Tabisola, "The use of saildrones to examine spring conditions in the bering sea: Vehicle specification and mission performance," in *Proc. OCEANS 2015-MTS/IEEE Washington*, 2015 pp. 1–6.

[11] J. R. Higinbotham, J. R. Moisan, C. Schirtzinger, M. Linkswiler, J. Yungel, and P. Orton, "Update on the development and testing of a new long duration solar powered autonomous surface vehicle," in *Proc. OCEANS*, 2008, pp. 1–10.

[12] H. Niu, Y. Lu, A. Savvaris, and A. Tsourdos, "Efficient path planning algorithms for unmanned surface vehicle," *IFAC-PapersOnLine*, vol. 49, no. 23, pp. 121–126, 2016.

[13] C. Whitt et al., "Future vision for autonomous ocean observations," *Front. Mar. Sci.*, vol. 7, 2020, Art. no. 697.

[14] R. Cavagnaro et al., "Powering the blue economy: Progress exploring marine renewable energy integration with ocean observations," *Mar. Technol. Soc. J.*, vol. 54, no. 6, pp. 114–125, 2020.

[15] R. Thom, S. Southard, and A. Borde, "Climate-linked mechanisms driving spatial and temporal variation in eelgrass (Zostera Marina l.) growth and assemblage structure in pacific northwest estuaries, USA," *J. Coastal Res.*, vol. 68, no. 1, pp. 1–11, 2014, doi: 10.2112/SI68-001.1.

[16] Z. Liu, Y. Zhang, X. Yu, and C. Yuan, "Unmanned surface vehicles: An overview of developments and challenges," *Annu. Rev. Control*, vol. 41, pp. 71–93, 2016. [Online]. Available: https://www.sciencedirect.com/science/article/pii/S1367578816300219

[17] P. H. Heins, B. L. Jones, and D. J. Taunton, "Design and validation of an unmanned surface vehicle simulation model," *Appl. Math. Modelling*, vol. 48, pp. 749–774, 2017. [Online]. Available: https://www.sciencedirect.com/science/article/pii/S0307904X17301245

[18] M. Paravisi, D. H. Santos, V. Jorge, G. Heck, L. M. Gonçalves, and A. Amory, "Unmanned surface vehicle simulator with realistic environmental disturbances," *Sensors*, vol. 19, no. 5, 2019, Art. no. 1068. [Online]. Available: https://www.mdpi.com/1424-8220/19/5/1068

[19] Z. Yang and T. Wang, "Tidal residual eddies and their effect on water exchange in puget sound," *Ocean Dyn.*, vol. 63, pp. 995–1009, 2013, doi: 10.1007/s10236-013-0635-z.

[20] Z. Yang, T. Wang, A. Copping, and S. Geerlofs, "Modeling of in-stream tidal energy development and its potential effects in tacoma narrows, Washington, USA," *Ocean Coastal Manage.*, vol. 99, pp. 52–62, 2014. [Online]. Available: https://www.sciencedirect.com/science/article/pii/S0964569114000477?via%3Dihub

[21] MathWorks Inc., "ScatteredInterpolant," Accessed: Mar. 2023. [Online]. Available: https://www.mathworks.com/help/matlab/ref/scatteredinterpolant.html

[22] K. D. Do and J. Pan, *Control of Ships and Underwater Vehicles*. Berlin, Germany: Springer, 2009.

[23] MathWorks Inc., "Control tutorials for MatLab & Simulink," Accessed on: Feb. 24, 2023. [Online]. Available: https://ctms.engin.umich.edu/CTMS/index.php?example=Introduction&section=ControlPID

[24] Q. Jiang, Y. Liao, Y. Li, and Y. Miao, "Heading control of unmanned surface vehicle with variable output constraint model-free adaptive control algorithm," *IEEE Access*, vol. 7, pp. 131008–131018, 2019.

[25] Y. Li, L. Wang, Y. Liao, Q. Jiang, and K. Pan, "Heading MFA control for unmanned surface vehicle with angular velocity guidance," *Appl. Ocean Res.*, vol. 80, pp. 57–65, 2018. [Online]. Available: https://www.sciencedirect.com/science/article/pii/S0141118718304462

[26] C. Lv, H. Yu, Z. Hua, L. Li, and J. Chi, "Speed and heading control of an unmanned surface vehicle based on state error PCH principle," *Math. Problems Eng.*, vol. 2018, 2018, Art. no. 9. [Online]. Available: https://www.hindawi.com/journals/mpe/2018/7371829/

[27] S. Hanif, R. J. Cavagnaro, Q. H. Nguyen, and M. J. E. Alam, "Simulation-based analysis of tidal energy system efficiency for powering at-sea applications," in *Proc. OCEANS 2021*, San Diego, Porto, 2021, pp. 1–7.

[28] P. Bachant and M. Wosnik, "Reynolds number dependence of cross-flow turbine performance and near-wake characteristics," *Proc. 2nd Mar. Energy Technol. Symp.*, 2014.

[29] MathWorks Inc., "PMSM field-oriented control," Accessed on: May 28, 2021. [Online]. Available: https://www.mathworks.com/help/sps/ref/pmsmfieldorientedcontrol.html

[30] Engineering Toolbox, "Drag coefficient," Accessed: Jun. 2023. [Online]. Available: https://www.engineeringtoolbox.com/drag-coefficient-d_627.html

[31] C. J. Rusch, T. R. Mundon, B. D. Maurer, and B. L. Polagye, "Hydrodynamics of an asymmetric heave plate for a point absorber wave energy converter," *Ocean Eng.*, vol. 215, 2020, Art. no. 107915. [Online]. Available: https://www.sciencedirect.com/science/article/pii/S002980182030874X

[32] National Oceanic and Atmospheric Association (NOAA), "Beaufort scale," Accessed: May 2024. [Online]. Available: https://www.weather.gov/pqr/beaufort

Linnea Weicht received the B.S. degree in mechanical engineering from Seattle Pacific University, Seattle, WA, USA, in 2019.

She is a Mechanical Engineer with Pacific Northwest National Laboratory, Seattle, focused on the development of marine energy technologies through simulation and testing.

Sarmad Hanif (Senior Member, IEEE) received the B.Sc. degree in electrical engineering from the University of Engineering and Technology Lahore, Lahore, Pakistan, in 2009, and the M.Sc. degree in power engineering and Ph.D. degree in electrical and electronics engineering from the Technical University of Munich, Munich, Germany, in 2013 and 2018, respectively.

He is currently a Technical Leader with the Electric Power Research Institute (EPRI), Washington, DC, USA. He has been involved in research activities on resilience, reliability, transactive energy systems, energy storage systems, and marine renewable energies. His research interests include power systems optimization, analysis, and economics.

Craig Bakker (Member, IEEE) received the Ph.D. degree in engineering from the University of Cambridge, Cambridge, U.K., in 2016.

His research focused on multidisciplinary design optimization with the University of Cambridge. He did postdoctoral research in climate change, food security, and economic modeling with Johns Hopkins University, Baltimore, MD, USA. He is currently a Research Scientist with the Pacific Northwest National Laboratory, Richland, WA, USA, where he has applied his expertise in game theory, AI/ML, and optimal control to biofuel supply chain modeling, counter-smuggling analysis, infrastructure modeling, synthetic biology, global food security, and climate science. His recent work has involved ML modeling techniques for deception-based attacks on commercial building heating, ventilation, and air conditioning systems, using operator theory to solve differential games, and quantifying the impacts of shocks to the global food supply chain.

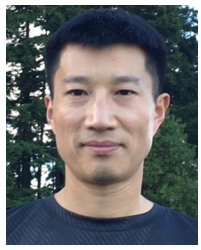

Taiping Wang received the Ph.D. degree in physical oceanography from the College of William & Mary, Williamsburg, VA, USA, in 2009.

He is currently a coastal modeler with the Coastal Sciences Division, Pacific Northwest National Laboratory, Richland, WA, USA. His research interests include numerical models to characterize tidal and wave energy resources in U.S. coastal waters, storm surge, and water quality modeling.

Nolann Williams received the M.Sc. degree in molecular biology from Washington State University, Pullman, WA, USA, in 2008, and M.S. degree in electrical engineering from California Polytechnic State University, San Luis Obispo, CA, USA, in 2018.

He is currently an Engineer specializing in early-stage R&D and productization. After working as a consultant for a diverse set of startups encompassing experimental weaponry, biomedical, and consumer products, he has served as a Research Engineer with the Pacific Northwest National Laboratory, Richland, WA, USA; Meta, Menlo Park, CA, USA; and A-M Systems, Sequim, WA. He focuses on the gray areas where engineering disciplines intersect and uses a passion for analog electronics, mechatronics, embedded systems, and system engineering to develop emerging technologies into useful products.

Robert J. Cavagnaro (Member, IEEE) received the B.S. degree in mechanical engineering from Carnegie Mellon University, Pittsburgh, PA, USA, in 2007, and the M.S. and Ph.D. degrees in mechanical engineering from the University of Washington, Seattle, WA, USA, in 2012 and 2016, respectively.

He is currently a Mechanical Engineer and Portfolio Manager with Marine and Coastal Research Laboratory, Pacific Northwest National Laboratory, Sequim, WA, USA, focused on the advancement of marine energy and robotics technologies.